DEVELOPMENT OF PLASMON ASSISTED NANOCOMPOSITE SEMICONDUCTOR MATERIALS FOR PHOTOCATALYTIC APPLICATIONS

A thesis submitted in partial fulfillment
of the requirements for the degree of
Doctor of Philosophy

Rajmoni Basumatary
Registration Number: PHY00369 of 2021-22

Faculty of Science and Technology
Department of Physics
Bodoland University, Kokrajhar- 783370
Assam, India

March, 2026

To my mother, my uncle, and my grandparents—
whose presence graced my journey from 1994 to 2021, leaving
warmth and love behind

DECLARATION BY THE CANDIDATE

The thesis titled "**Development of plasmon assisted nanocomposite semiconductor materials for photocatalytic applications"** is being submitted to the Bodoland University in partial fulfilment for the award of the degree of Doctor of Philosophy in Physics is a record of original research work accomplished by me under the supervision of Dr. Anjalu Ramchiary, Assistant Professor, Department of Physics, Bodoland University, Kokrajhar, Assam, India.

The assistance and support extended to me from various sources have been appropriately acknowledged.

No part of this thesis has been submitted elsewhere for award of any other degree.

Date: 19-03-2026
Place: Kokrajhar

(Rajmoni Basumatary)
Reg. No.: PHY00369 of 2021-22
Department of Physics
Bodoland University, Kokrajhar
Assam, India

DEPARTMENT OF PHYSICS
BODOLAND UNIVERSITY
Kokrajhar-783370, BTR, Assam
www.bodolanduniversity.ac.in

Dr. Anjalu Ramchiary
Assistant Professor
Department of Physics
Email:anjalu1417@buniv.edu.in
Mobile: +91-8812871635

CERTIFICATE OF THE SUPERVISOR

This is to certify that the thesis titled, "**Development of plasmon assisted nanocomposite semiconductor materials for photocatalytic applications**" submitted to the Bodoland University in the Department of Physics under the Faculty of Science and Technology, for fulfilment of the award of the degree of Doctor of Philosophy in Physics is a record of original research work carried out by Rajmoni Basumatary under my personal supervision and guidance. He has complied with all the requirements as laid down in the regulations of Bodoland University for the award of Doctor of Philosophy in Physics.

He has duly recorded his acknowledgements for all forms of assistance received from different sources.

No part of this thesis has been reproduced elsewhere for award of any other degree.

Date: 19-03-2026
Place: Kokrajhar

(Dr. Anjalu Ramchiary)
Assistant Professor
Department of Physics
Bodoland University, Kokrajhar
Assam, India

Acknowledgement

First and foremost, I extend my deepest gratitude to my supervisor, Dr. Anjalu Ramchiary, Assistant Professor in the Department of Physics at Bodoland University, for his exceptional mentorship and profound expertise in the subject. His unwavering dedication to research and his remarkable ability to discern critical relationships between variables have been a constant source of inspiration. His guidance motivated me to emulate his work ethic and persevere with determination throughout this endeavour. His timely validation and insightful feedback were instrumental to the successful completion of this study.

I would also like to acknowledge all the DRC members, including Prof. Heremba Bailung (HOD/Chairperson), Dr. Anjalu Ramchiary (Guide), Dr. Prince Kumar Mochahari (Associate Professor), Dr. Rajeeb Brahma (Assistant Professor), and Dr. Kalyan Dey (Assistant Professor) of the Department of Physics, Bodoland University, and the Dean (Faculty of Science & Technology); the RAC members: Prof. Sanjay Basumatary, Department of Chemistry, Bodoland University, and Dr. Rebecca Daimary, Department of Botany, Bodoland University; and other field experts for their valuable feedback and insightful advice on my work reports.

I am also privileged to have worked in the nurturing academic environment fostered by the Department of Physics, Bodoland University. The collegiality, integrity, and diligence of the faculty members, non-teaching staff, and fellow research scholars significantly enriched my experience. I also extend my sincere gratitude to the administrative authorities of Bodoland University for their consistent support, responsiveness, and guidance.

I express my sincere gratitude to all my research collaborators, Dr. Dimpul Konwar, Dr. Bablu Basumatary, Phulmani Basumatary, and Saurabh J. Hazarika, whose contributions are permanently etched in the publications we co-authored. Their collaboration was invaluable to the progression of my work.

With immense gratitude, I acknowledge DST-SERB for funding a research project during the early phase of my doctoral journey. This support enabled access to essential instruments required for experimental research. I also extend my sincere thanks to the Ministry of Tribal Affairs for awarding me with NFST 2021-2022 PhD-

fellowship. I am also thankful to all the research institutions (SAIC-IASST, SAIC-TU, NECBH-IIT GHY, SAIC-NEHU, CIF-IIT GHY, NIT Silchar) whose facilities I utilized for sample characterization. Their infrastructure was crucial for the technical aspects of this work.

I would also like to express my heartfelt gratitude to my family and friends, both within and outside the university, who have been a part of my journey and have uplifted me in countless ways. I am especially thankful to Onsar Brahma, Omkar Brahma, Samudra Brahma, Kundan Brahma, Mwikhwm Narzary, Rishang Brahma, Sanswrang Basumatary, Indra Bhushan Basumatary, Mwina Basumatary, and Sujata Brahma, for their emotional and technical support, as well as their camaraderie. The thoughtful conversations during our breaks and the occasional weekend retreats were not only refreshing but also a great source of encouragement and motivation.

Lastly, I offer my heartfelt and most personal gratitude to my late mother, Smt. Anu Basumatary, who departed for her heavenly abode shortly after my selection into the PhD programme. Her unwavering support and encouragement during my most challenging times were the foundation of my journey. She was the cornerstone of our family, and it was under the shade of her wisdom and unconditional love that I grew from a fragile sapling into a tree grounded in strength and resilience.

Regards,

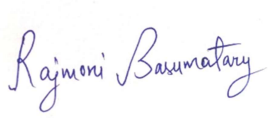

List of Figures

Figure	Title	Page No.
Figure 1.1	Water distribution on Earth.	1
Figure.1.2	Pie chart representation of water pollution sources.	2
Figure 1.3	Graph showing the percentage increase in water usage across different sectors.	2
Figure 1.4	Classification of water purification techniques.	4
Figure 1.5	Illustration of semiconductor photocatalysis.	7
Figure 1.6	Bar chart showing the annual number of Scopus-indexed publications on photocatalysis from 2010 to 2025.	8
Figure 1.7	Solar spectrum showing the distribution of energy versus wavelength.	8
Figure 1.8	Map showing horizontal solar irradiance across different regions of the world.	9
Figure 1.9	Illustration of horizontal solar irradiance levels across different regions of India.	10
Figure 1.10	Classification of different types of heterojunctions.	18
Figure 1.11	Local surface plasmon resonance on a spherical nanoparticle	21
Figure 1.12	Illustration of a plane-wave light incident on a uniform spherical nanoparticle with diameter (R) and a complex frequency-dependent dielectric constant $\varepsilon(\omega)$. The external electric field $\vec{E}$ exerts a force on the free electrons within the nanosphere, resulting in the formation of an induced electric dipole.	22
Figure 1.13	Schematic illustration of a semiconductor–metal Schottky junction with parabolic DOS. Light-induced hot electrons with energies exceeding the Schottky barrier are injected from the plasmonic metal into the conduction band of the semiconductor.	23
Figure 1.14	Mechanisms of charge separation in various photocatalytic	25

nanostructures.
Figure 1.15 Band edge positions of some relevant semiconductor photocatalysts. 30
Figure 2.1 Illustration of sol-gel method. 49
Figure 2.2 Illustration of modified sol-gel method. 50
Figure 2.3 Illustration of co-precipitation method. 51
Figure 2.4 Illustration of reduction method. 51
Figure 2.5 Illustration of centrifugation process. The solid sample particles are forced down to accumulate at the bottom of centrifuge tube by centrifugal force, after which the unwanted liquid is removed using a micropipette 52
Figure 2.6 Schematic diagram of tube furnace with the sample placed inside. 53
Figure 2.7 Mortar and pestle. 53
Figure 2.8 Illustration of ultrasonication. A sample in a suitable solvent is placed in a ultrasonicator bath 54
Figure 2.9 Bragg's law of X-ray diffraction. 55
Figure 2.10 Schematic diagram of SEM. 57
Figure 2.11 Schematic diagram of TEM. 58
Figure 2.12 Illustration of SAED pattern. 58
Figure 2.13 Energy diagram showing various transitions that produces photoluminescence. 60
Figure 2.14 Illustration of Beer-Lambert's law. 61
Figure 2.15 Inside view of reactor set-up 64
Figure 2.16 Energy spectrum (Intensity vs wavelength) of SANSI LED bulb 64
Figure 3.1 Block diagram illustrating the synthesis of Co-doped TiO_2 step by step. 67
Figure 3.2 X-ray diffraction spectra of T400, CT400, CT600, and CT700. 69
Figure 3.3 XRD spectra of pristine TiO_2 calcined at 600 ^{o}C (T600) and 700 ^{o}C (T700). 70

Figure 3.4 X-ray diffraction spectrum of $TiO_2/CoTiO_3$ with 20 wt% Co. 70
Figure 3.5 (a) Optical absorbance spectra, (b) bandgap determination, and (c) magnified y-axis data of T400, CT400, CT600, and CT700 photocatalysts. 72
Figure 3.6 Determination of n value by plotting $\ln(\alpha.h\nu)$ vs. $\ln(h\nu - E_g)$ graph 73
Figure 3.7 SEM images of (a) T400 and (b) CT600, along with their magnified view of the selected area. EDX of (c) T400, and (d) CT600 with atomic composition. 74
Figure 3.8 TEM and high-resolution TEM (a, b) T400 and (c, d) CT600. (e) SAED pattern with the lattice planes and (f) particle distribution of CT600. 75
Figure 3.9 ESR spectra of (a) T400, (b) CT400, and (c) CT600 photocatalysts at room temperature. 77
Figure 3.10 (a) Photoluminescence spectra of T400, CT400, and CT600 photocatalysts at room temperature, (b-d) Gaussian fitting of each PL spectrum of T400, CT400, and CT600 78
Figure 3.11 XPS spectra of T400, CT400, and CT600. (a) Full survey profile, (b) Ti 2p spectra, (c) O 1s spectra, and (d) Co 2p spectra. 80
Figure 3.12 XPS peak fitting: Ti 2p spectrum of (a) T400, (b) CT400 and (c) CT600. O1s spectra of (d) T400, (e) CT400 and (f) CT600. Co 2p spectra of (g) CT400 and (h) CT600. 81
Figure 3.13 (a) Photocatalytic degradation profile (C/C_o vs. time) of MB under visible light (0 to 90 min) using T400, CT400, CT600, and CT700 photocatalysts. (b) ln (C/C_o) vs. time plot to measure the rate constant, (c) Optical images of MB degradation using T400, CT400, CT600, and CT700 photocatalysts, after visible light exposure for 90 min. 84
Figure 3.14 Absorption spectra of MB degradation with time using (a) T400, (b) CT400, (c) CT600, and (d) CT700. The 85

maximum absorption at wavelength 664 nm was recorded. About 97% degradation of MB by Co-TiO_2/$CoTiO_3$ photocatalyst (CT600) in 90 min was observed.

Figure 3.15 (a) Photocatalytic degradation profile (C/C_o vs. time) of MB using T600 and T700 and (b) ln C/Co vs. time plot to measure the rate constant. 86

Figure 3.16 Photocatalytic mechanism of Co-TiO_2/$CoTiO_3$ (CT600) photocatalyst. Interfacial junctions between (a) $CoTiO_3$-rutile-anatase phase and (b) $CoTiO_3$-anatase-rutile phase of TiO_2. 87

Figure 4.1 Block diagram illustrating the synthesis of Ag@Cu_2O-CuO/TiO_2 97

Figure 4.2 XRD patterns of TiO_2, CuO, CuO/TiO_2, and Ag@Cu_2O-CuO/TiO_2. 98

Figure 4.3 X-ray diffraction spectra of Cu_2O (as-prepared), Ag@CuO calcined at 600 ^oC, and Ag@TiO_2 calcined at 600 ^oC. 99

Figure 4.4 (a) UV-vis-DRS of TiO_2, CuO, CuO/TiO_2 and Ag@Cu_2O-CuO/TiO_2, and UV-vis absorbance spectra of bulbous Ag (b) Bandgap determination of TiO_2, CuO, CuO/TiO_2 and Ag@Cu_2O-CuO/TiO_2 using Tauc plot. 100

Figure 4.5 (a) UV-vis-DRS of Cu_2O (as-prepared), Ag@CuO (600 ^oC), and Ag@TiO_2 (600 ^oC). (b) Bandgap determination using Tauc plot. 101

Figure 4.6 (a) Raman, and (b) room temperature ESR spectra, of TiO_2, CuO/TiO_2, Ag@Cu_2O-CuO/TiO_2. 103

Figure 4.7 Photoluminescence spectra of TiO_2, CuO, CuO/TiO_2, and Ag@Cu_2O-CuO/TiO_2. 104

Figure 4.8 (a) XPS measurements (full survey profile) of various catalysts. XPS peak fitting: Ti 2p spectra of (b) TiO_2, (c) CuO/TiO_2, and (d) Ag@Cu_2O-CuO/TiO_2. 105

Figure 4.9 XPS spectra of Ag@CuO and Ag@TiO_2 (full survey 106

profile).

Figure 4.10 XPS peak fitting: O 1s spectra of (a) TiO_2, (b) CuO, (c) CuO/TiO_2, and (d) $Ag@Cu_2O$-CuO/TiO_2. 107

Figure 4.11 XPS peak fitting Cu 2p spectra of (a) CuO, (b) CuO/TiO_2, (c) $Ag@Cu_2O$-CuO/TiO_2, and (d) XPS scanning of Ag 3d. 108

Figure 4.12 Ag 3d XPS spectra of (a) $Ag@TiO_2$, and (b) Ag@CuO. 109

Figure 4.13 XPS spectra of Ag@CuO and $Ag@TiO_2$ (a) Ti 2p spectra, (b) Cu 2p spectra and (c-d) O 1s spectra. 110

Figure 4.14 Valence band XPS spectra of TiO_2, CuO, and Cu_2O. 111

Figure 4.15 FE-SEM image of (a-b) Ag, (c) TiO_2, (d) CuO, (e) CuO/TiO_2, and (f) $Ag@Cu_2O$-CuO/TiO_2. 112

Figure 4.16 TEM and HR-TEM images of (a-b) Ag, (c) TiO_2, (d-e) CuO, (f-g) CuO/TiO_2, and (h-i) $Ag@Cu_2O$-CuO/TiO_2. 113

Figure 4.17 (a) Photocatalytic degradation profile (C/C_o vs. time) of MB under visible light using different photocatalysts, (b) ln C/C_o vs. time plot to determine the rate constant. 115

Figure 4.18 Absorption spectra of MB degradation with time using (a) TiO_2, (b) CuO, (c) CuO/TiO_2, and (d) $Ag@Cu_2O$-CuO/TiO_2. 116

Figure 4.19 (a) Photocatalytic degradation profile (C/C_o vs. time) of MB under visible light using $Ag@TiO_2$ and Ag@CuO, (b) ln C/C_o vs. time plot to determine the rate constant. 116

Figure 4.20 (a) Photocatalytic degradation profile (C/C_o vs. time) of phenol under visible light using TiO_2, CuO/TiO_2, and $Ag@Cu_2O$-CuO/TiO_2, and (b) ln C/C_o vs. time plot to determine the rate constant. 117

Figure 4.21 (a) Repeatability test of $Ag@Cu_2O$-CuO/TiO_2 photocatalyst, and (b) ln C/C_o vs. time plot to determine the rate constant. 118

Figure 4.22 (a) Photocatalytic degradation of MB and (b) degradation percent by $Ag@Cu_2O$-CuO/TiO_2 photocatalyst with various scavenging agents. 120

Figure 4.23	Photocatalytic mechanism of $Ag@Cu_2O$-CuO/TiO_2 photocatalyst: interfacial junctions between CuO-TiO_2-Cu_2O phase.	122
Figure 5.1	Block diagram illustrating the synthesis of $Ag@NiO/Ag_2CrO_4$.	134
Figure 5.2	X-ray diffraction spectra of NC, AC, and ANC.	136
Figure 5.3	X-ray diffraction spectra of raw Ni-Cr LDH and Ag@Ni-Cr LDH.	136
Figure 5.4	(a) UV-Vis DRS of NC, AC, ANC, and UV-Vis absorbance spectrum of Ag. (b) Bandgap determination using Tauc plot.	138
Figure 5.5	(a) X-ray diffraction spectra of AN (Ag@NiO), (b) UV-visible DRS spectrum of AN and (c) Band gap determination of AN using Tauc plot.	139
Figure 5.6	(a) Raman and (b) photoluminescence spectra of NC, AC, and ANC.	140
Figure 5.7	XPS spectra (full survey profile) of ANC.	141
Figure 5.8	XPS peak fit of ANC: (a) Ni 2p spectra, (b) Cr 2p, (c) O 1s, and (d) Ag 3d.	142
Figure 5.9	Valence band XPS spectra of ANC.	144
Figure 5.10	SEM images of (a-b) NC snd (c-d) ANC.	144
Figure 5.11	(a-d) TEM images of NC.	145
Figure 5.12	TEM images of (a-c) ANC, and (d) SAED pattern of ANC.	146
Figure 5.13	(a-b) High resolution-TEM images of ANC.	147
Figure 5.14	(a-d) TEM images of Ag nanoparticles (at different magnifications).	148
Figure 5.15	EDX plot of (a) NC and (b) ANC photocatalysts along with the table showing the atomic composition and percentage.	149
Figure 5.16	(a) Photocatalytic degradation pattern (C/C_o vs. time) of MB upon visible light exposure (0 to 90 min) using NC,	150

AC, and ANC photocatalyst, (b) ln C/C_o against time plot to determine the rate constant.

Figure 5.17 Absorption spectra of MB recorded for a total duration of 90 min light irradiation in the presence of (a) NC, (b) AC, and (c) ANC photocatalysts. 151

Figure 5.18 Photographic representation of MB degradation, captured at 15-minute intervals during visible-light irradiation of the MB solution containing the ANC photocatalyst, from 0 to 90 minutes. 152

Figure 5.19 Absorption spectra of RhB recorded for a total duration of 90 min light irradiation in the presence of (a) NC and (b) ANC photocatalysts. 153

Figure 5.20 (a) Photocatalytic degradation pattern (C/C_o vs. time) of RhB upon visible light exposure (0 to 90 min) using NC and ANC photocatalyst, (b) ln C/C_o vs. time graph. 154

Figure 5.21 MB removal efficiency of the ANC photocatalyst over three consecutive photocatalytic cycles. 155

Figure 5.22 (a) MB degradation over time and (b) degradation efficiency (%), achieved by the ANC photocatalyst in the presence of different scavenging agents. 156

Figure 5.23 Mott–Schottky plots of counterparts (a) NiO, (b) AC, and composite (c) ANC. 158

Figure 5.24 Proposed photocatalytic mechanism of ANC photocatalyst (a) before and (b) after heterojunction. A p-n heterojunction with Z-scheme charge transfer dynamics, facilitated by plasmonic Ag via the PIRET mechanism. 159

Figure 5.25 Time-resolved photoluminescence spectra of NC, AC, and ANC 162

Figure 6.1 (a) XRD spectra of $Ag@TiO_2$ calcined at 600 ºC prepared with different Ag shapes and (b) photocatalytic degradation profile (C/C_0 vs. time) of MB using the samples under visible light. 177

Figure 6.2 (a) ln C/C_0 vs. time plot to determine the rate constant of the MB degradation using $Ag@TiO_2$ calcined at 600 ºC prepared with different Ag shapes, (b) bar chart representing the dye degradation capabilities of the photocatalysts. 179

Figure 6.3 (a) XRD spectra of $Ag@TiO_2$ calcined at 600 ºC prepared with different Ag concentration and (b) photocatalytic degradation profile (C/C_0 vs. time) of MB using the samples under visible light. 180

Figure 6.4 (a) ln C/C_0 vs. time plot to determine the rate constant of the MB degradation using $Ag@TiO_2$ calcined at 600 ºC prepared with different Ag loading, (b) bar chart representing the dye degradation capabilities of the photocatalysts. 181

Figure 6.5 (a) XRD spectra of $Ag@TiO_2$ with 10 mL cubical Ag loading, calcined at different temperatures and (b) photocatalytic degradation profile (C/C_0 vs. time) of MB using the samples under visible light. 183

Figure 6.6 (a) ln C/C_0 vs. time plot to determine the rate constant of the MB degradation using $Ag@TiO_2$ photocatalysts with 10 mL cubical Ag loading, calcined at different temperatures, (b) bar chart representing the dye degradation capabilities of the photocatalysts. 184

Figure 6.7 (a) X-ray diffraction spectra of different $Ag@TiO_2$ photocatalysts having rutile phases and (b) photocatalytic degradation profile (C/C_0 vs. time) of MB using the samples under visible light. 185

Figure 6.8 (a) ln C/C_0 vs. time plot to determine the rate constant of the MB degradation using different $Ag@TiO_2$ photocatalysts having rutile phases, (b) bar chart representing the dye degradation capabilities of the photocatalysts. 186

Figure 6.9	(a) UV-vis DRS of Ag@TiO_2(S), Ag@TiO_2(C), Ag@TiO_2(B); and UV-vis absorbance spectra of spherical, cubical and bulbous Ag, (b) bandgap determination of the photocatalysts.	188
Figure 6.10	(a) UV-DRS of Ag@TiO_2(C) calcined at various temperatures, (b) bandgap determination using Tauc plot.	189
Figure 6.11	(a-d)TEM images of Ag(S).	190
Figure 6.12	(a-b)TEM images of Ag(C).	191
Figure 6.13	(a-d) TEM images of Ag(B).	191
Figure 6.14	TEM images of (a) Ag(S), (b-d) Ag@TiO_2(S).	193
Figure 6.15	(a) HRTEM image and (b) SAED pattern of Ag@TiO_2(S).	193
Figure 6.16	TEM images of (a) Ag(C) and (b-d) Ag@TiO_2(C).	194
Figure 6.17	(a-c) HRTEM images, and (d) SAED pattern of Ag@TiO_2(C).	195
Figure 6.18	(a-b) FESEM, (c) TEM images of Ag(B), and (d) TEM image of Ag@TiO_2(B).	196
Figure 6.19	(a-c) HRTEM images and (d) SAED pattern of Ag@TiO_2(B).	197
Figure 6.20	SEM images of (a) Ag@TiO_2(S), (b) Ag@TiO_2(C20), (c) raw Ag@TiO_2(C20), (d) Ag@TiO_2(C10), (e) Ag@TiO_2(C5), and (f) raw Ag@TiO_2(C5).	198
Figure 6.21	(a-d) SEM images of Ag@TiO_2(C10) at different magnifications	198
Figure 6.22	Raman spectra of Ag@TiO_2 (prepared with different Ag shapes) and pristine TiO_2 calcined at 600 ºC.	199
Figure 6.23	Photoluminescence spectra of Ag@TiO_2 (prepared with different Ag shapes) and pristine TiO_2 calcined at 600 ºC.	201
Figure 6.24	(a) XPS survey profile of Ag@TiO_2(C), XPS peak fit of Ag@TiO_2(C): (b) Ti 2p spectra, (c) O 1s, and (d) Ag 3d	202

List of Tables

Tables	Title	Page No.
Table 3.1	Transitional energy and crystallite size of the as-prepared photocatalysts.	74
Table 3.2	XPS peak positions and areas of Ti 2p, Ti O1s, and Co 2p for T400, CT400 and CT600 photocatalysts.	82
Table 3.3	Rate constant of MB degradation using various photocatalyst	86
Table 4.1	Rate of degradation of MB using different photocatalysts under visible light.	119
Table 4.2	Rate constants, quenching agents and amount, and active radicals.	120
Table 5.1	Rate constant and regression coefficient for MB degradation	152
Table 6.1	Rate of MB degradation using Ag@TiO_2 photocatalysts calcined at 600 ºC prepared with different shapes	180
Table 6.2	Rate of MB degradation using Ag@TiO_2 photocatalysts calcined at 600 ºC prepared with different concentration of cubical Ag nanoparticles	183
Table 6.3	Rate of MB degradation using Ag@TiO_2 photocatalysts with 10 mL cubical Ag loading, calcined at different temperatures	184
Table 6.4	Rate of MB degradation using different Ag@TiO_2 photocatalysts having rutile phases	186

Abbreviation

AOPs	:Advanced Oxidation Processes
BOD	:Biological Oxygen Demand
COD	:Chemical Oxygen Demand
UV	:Ultraviolet
NIR	:Near-infrared
KWh	:Kilo Watt hour
CB	:Conduction Band
VB	:Valence Band
STM	:Scanning Tunneling Microscopy
ROS	:Reactive Oxygen Species
BTBT	:Band-to-band Tunneling
LSPR	:Local Surface Plasmon Resonance
SPR	:Surface Plasmon Resonance
DET	:Direct electron transfer
DOS	:Density of states
PIRET	:Plasmon-induced resonant energy transfer
RET	:Resonant energy transfer
LEMF	:Localized electromagnetic field enhancement
TD-OFDFT	:Time-dependent orbital-free density functional theory
NHE	:Normal Hydrogen Electrode
E_{vac}	:Vacuum energy level
eV	:electron-Volt
DD	:Doubly distilled

RPM	:Rotations per minute
ºC	:Degree Celsius
hrs	:hours
Å	:Angstrom
XRD	:X-ray Diffraction
D	:Crystallite size
d	:Interplanar spacing
λ	:Wavelength of the X-ray radiation (Cu Kα =0.15406nm)
k	:The shape factor (0.9)
β	:Full width at half maxima
θ	:The diffraction angle
SEM	:Scanning Electron Microscopy
FESEM	:Field-emission Scanning Electron Microscopy
TEM	:Transmission Electron Microscopy
HRTEM	:High Resolution Transmission Electron Microscopy
EDX	:Energy Dispersive X-ray spectroscopy
SAED	:Selected Area Electron Diffraction
PL	:Photoluminescence Spectroscopy
UV-vis-DRS	:UV-visible-diffuse reflectance spectroscopy
XPS	:X-ray photoelectron spectroscopy
ESR	:Electron Spin Resonance
EIS	:Electrochemical Impedance Analysis
LED	:Light emitting diode
h^+	:holes

e^-	:electrons
$^{\bullet}O_2^-$	:Superoxide radicals
$^{\bullet}OH$	:Hydroxyl radicals
$^1O_2$	:Singlet oxygen
AO	:Ammonium Oxalate
SN	:Silver Nitrate
BQ	:p-benzoquinone
IPA	:Isopropyl alcohol
LH	:L-histidine
MB	:Methylene Blue
RhB	:Rhodamine B
h	:Plank Constant
ν	:Frequency of Photon
α	:Extinction coefficient
E_g	:Bandgap energy
E_{fb}	:Flat band energy
E	:Energy
E_V	:Valence band maximum energy
E_C	:Conduction band minimum energy
E_{NHE}	:Potential of standard hydrogen electrode
M	:Molarity
mM	:Milli mol
nm	:Nanometer
k	:Rate constant

t	:Time
C	:Final concentration
C_o	:Initial concentration
min	:minute
PEC	:Photoelectrochemical
FTO	:Fluorine-doped tin oxide
MO	:Methyl orange
β	:Bohr magnetron
H_o	:Resonance Magnetic Field
BE	:Binding Energy
VBM	:Valence band maximum
CBM	:Conduction band minimum
LDH	:Layered Double Hydroxides